Sensors & Actuators: A. Physical 376 (2024) 115552

Contents lists available at ScienceDirect

Sensors and Actuators: A. Physical

journal homepage: www.journals.elsevier.com/sensors-and-actuators-a-physical

$Ni_{80}Fe_{20}$ thickness optimization of magnetoplasmonic crystals for magnetic field sensing

D.V. Murzin [a,*], V.K. Belyaev [a], K.A. Mamian [b], F. Groß [c], J. Gräfe [c], A.Y. Frolov [b], A.A. Fedyanin [b], V.V. Rodionova [a]

[a] Immanuel Kant Baltic Federal University, Kaliningrad 236041, Russia
[b] Lomonosov Moscow State University, Moscow 119991, Russia
[c] Max Planck Institute for Intelligent Systems, Stuttgart 70569, Germany

ARTICLE INFO

Keywords:
Transverse Kerr effect
Surface plasmon-polariton
Magnetoplasmonic crystal
Magnetic field sensor

ABSTRACT

A promising approach to enhance the transverse Kerr effect with potential applications in the detection of weak magnetic fields is the use of magnetoplasmonic crystals based on ferromagnetic metals. The sensitivity, measuring field range, and limit-of-detection of 1D magnetoplasmonic crystals with 5–20 nm thick $Ni_{80}Fe_{20}$ layers are analyzed in this study based on magnetic, optical, and magneto-optical characterization. The magnetoplasmonic crystal with 10 nm-thick $Ni_{80}Fe_{20}$ layer provided a sensitivity of 21.9 μV/mOe, a limit-of-detection of 3.6 mOe, and a measuring field range of 1.134 Oe. This sample was also utilized as a magnetic field probe to reconstruct the magnetic configuration of a multicore cable and a planar induction coil, thereby highlighting its potential for the visualization of DC magnetic fields.

1. Introduction

In today's technological landscape, the prioritization of energy efficiency in miniaturized electromagnetic and micromagnetic devices has put an increased emphasis on remote monitoring of their performance through their magnetic state. Moreover, the ability to reconstruct the magnetic field distribution of individual electronic components enables real-time monitoring and facilitates the timely detection of failures. A well-known method employed to achieve this task is measuring the magnetic field generated within such systems using encircling or proximity-based magnetic field sensors [1]. While the market offers different magnetic field sensing concepts, the most commercially appealing options involve Hall effect, fluxgate, magnetoimpedance, and magnetoresistive sensors, known for their cost-effectiveness and sub-millioersted sensitivity potential [2,3]. These sensors can be integrated directly into devices for magnetic field monitoring, translating applied magnetic flux into electronic signals induced in the contact pads through the utilization of electronic read-out schemes. However, to address the growing demand for contactless sensing mechanisms not susceptible to electromagnetic interference, the adoption of magnetometers featuring optical readout capabilities can prove highly advantageous. Currently, the most sensitive optical magnetometers utilize the unique properties of alkali vapor cells or nitrogen-vacancy centers in diamonds, employing sophisticated detection protocols to achieve cutting-edge picooersted sensitivity and nanometer-scale resolution [4,5]. Although these sensors have great potential for research, biomedical applications, and space exploration, it seems impractical to use them in sectors that require cost-effective and simple solutions. An alternative approach that provides simplicity, accessibility, and the convenience of remote optical read-out involves the use of magneto-optical sensors.

The magneto-optical effects, which are a fascinating and significant phenomenon in modern physics, are characterized by a modification in the polarization or intensity of light when it interacts with magnetic materials [6–8]. Over the years, a variety of research efforts have been dedicated to exploring the possible applications of these effects in various devices, including magnetic field sensors [9]. One notable example of such a sensor is the rare-earth iron garnet magneto-optical indicator film, which has been extensively studied for its ability to provide precise and comprehensive measurements of magnetic fields [10–13]. Due to their versatility, magneto-optical sensors have the potential to be integrated into a wide range of industrial processes for quantitative measurement and visualization of magnetic fields. Table 1

Significant progress has been made in improving the sensitivity and finding new application areas of magneto-optical sensors by using

* Corresponding author.
E-mail address: murzindmitri@gmail.com (D.V. Murzin).

https://doi.org/10.1016/j.sna.2024.115552
Received 12 March 2024; Received in revised form 7 May 2024; Accepted 4 June 2024
Available online 5 June 2024

plasmonic structures known as magnetoplasmonic crystals (MPCs) [14–16]. MPCs can enhance magneto-optical effects by several orders of magnitude due to the excitation of surface plasmon-polaritons – electromagnetic waves coupled to the collective oscillations of the free charges at the metal/dielectric interface. For instance, MPCs composed of an iron garnet film and a gold diffraction grating have demonstrated a sensitivity of 2 nT/Hz$^{1/2}$ utilizing the longitudinal magneto-photonic intensity effect in the light transmission geometry [17]. However, in situations where proximity to a magnetic object is necessary, the transmission geometry of the sensing elements may not always be suitable. To overcome this challenge, MPCs utilizing the enhanced transverse Kerr effect (δ) can be used, operating in the reflection geometry and allowing for placement in close proximity to a magnetic field source [18]. These sensing elements are made of plasmonic materials combined with metallic ferromagnetic films often made of iron, nickel, cobalt, or their alloys to optimize light absorption losses, magnetic anisotropy and damping, and δ value in relatively low magnetic fields [19–22]. The operational concept of these sensing elements relies on the demagnetization dynamics of the MPCs under the AC magnetic field [23]. By gradually reducing the magnitude of the AC field to zero and registering the magneto-optical response, a calibration curve can be obtained. This curve, in conjunction with the magnetic characterization of the MPC, can be used to determine the sensitivity, the modulation field required for operation (H_{mod}), and the measuring field range (ΔH). It is also a tool for recalibrating the strength of an applied external magnetic field (H_{ext}) affecting the modulation of the MPC's magnetization by the H_{mod}.

Both hard and soft magnetic materials can be used in the MPCs to fulfill specific criteria, such as a low H_{mod} of 5.1 Oe [24] to avoid its influence on the experimental objects' magnetic state, or a high limit-of-detection (*LoD*) of 10^{-6} Oe for accurate measurements of weak magnetic fields [23]. However, those achievements are accompanied by a reduction in ΔH, which is also a crucial parameter for sensing applications [25]. To tackle this challenge, an efficient strategy for enhancing the ΔH of the MPC-based magnetic field sensor involves adjusting the thickness of its ferromagnetic layer. This approach enables modification of MPCs' optical and magnetic properties, leading to alterations in the shape and magnitude of the calibration curve without compromising essential aspects of the sensor's performance. In particular, the use of thin ferromagnetic layers allows for significant reduction in the H_{mod}, thereby improving the energy efficiency of the sensing elements based on MPCs [19,24,26].

In the current study, the potential of 1D MPCs based on $Ni_{80}Fe_{20}$ films with thicknesses ranging from 5–20 nm as magnetic field probes is being assessed. Through the utilization of magnetometry, and spectroscopy in the visible spectral range, the MPCs' sensitivity, ΔH, *LoD,* and limit-of-quantification (*LoQ*) were determined. It was found that the decrease in the $Ni_{80}Fe_{20}$ layer thickness enhances the H_{mod}, sensitivity, and *LoD* of the MPCs while simultaneously diminishing the optimal ΔH. The MPC based on the 10 nm-thick $Ni_{80}Fe_{20}$ layer provided the optimal parameters and was employed to visualize 2D magnetic field maps of a multicore cable and a planar induction coil.

2. Materials and methods

The substrates used for MPCs fabrication were 1D polycarbonate quasi-sinusoidal diffraction gratings with a period of 320 nm and groove depth of 20 nm. These substrates were coated with 50 nm layer of Ag, followed by 10, 15, or 20 nm layer of $Ni_{80}Fe_{20}$, and finally 10 nm layer of Si_3N_4. The coating was conducted using the ORION-8-UHV DC magnetron sputtering setup by AJA International. A soft magnetic $Ni_{80}Fe_{20}$ was chosen to due to its small magnetic damping, low magnetic anisotropy, and relatively low losses compared to other ferromagnetic metals, while the Ag and Si_3N_4 layers served as protective layers to prevent oxidation of the ferromagnetic layer. The thickness of the Ag layer was chosen to be significantly thicker than the penetration depth of light to prevent the influence of the substrate material on the materials' optical and magneto-optical properties. To ensure the desired thickness of each layer, the sputtering time was adjusted based on precalculated sputtering rates, with monitoring being carried out using the Inficon SQM-160 quartz microbalance sensor. The sputtering process took place under room temperature at a pressure of 3 mTorr within an argon atmosphere. A source power of 75 W and an argon flow rate of 6 sccm were maintained throughout the process. The reference samples for optical and magneto-optical characterization based on Si (400) wafers were prepared in the same deposition cycles. Fabrication protocol for the MPC based on the 5 nm-thick $Ni_{80}Fe_{20}$ layer was the same, as shown in Ref. [24]. Composition verification of the samples was done using the SEM TM4000II by Hitachi equipped with the EDX system Quantax 75 by Bruker. An example of the obtained EDX spectra and estimated composition of the MPC based on a 20 nm-thick $Ni_{80}Fe_{20}$ layer can be found in Fig. S1 of the supplementary materials. Post-deposition, the morphology and period of the diffraction gratings were preserved according to the AFM images obtained for each MPC using the AFM NTEGRA AURA in a semi-contact mode. The AFM images of the MPCs are provided in Fig. S2 of the supplementary materials.

To study the magnetic properties of the MPCs, hysteresis loops were measured along the easy magnetization axis (EMA) using the NanoMOKE 3 magneto-optical magnetometer in the longitudinal magneto-optical Kerr effect geometry (MOKE). These measurements were carried out at the center of the MPCs in a spot with a diameter of 5 μm. The obtained curves were used to determine the coercive field (H_c) and saturation field (H_{sat}) values of the MPCs. Additionaly, local hysteresis loops along the EMA were measured using the Evico Magnetics magneto-optical Kerr microscope & magnetometer in the transverse geometry of the applied field. The in-plane magnetic properties of the MPCs, both along and perpendicular to the EMA, were also studied using the vibrating sample magnetometer (VSM) LakeShore 7404i. Unlike the MOKE measurements, which are confined to a specific area determined by the laser spot size and light penetration depth, the VSM technique allowed to study the magnetic properties across the entire volume of the MPCs.

The reflectivity (R_0) of the MPCs and reference samples was analyzed under *p*-polarized light within the spectral range of 500 – 700 nm at an incidence angle $\theta = 68^\circ$. This angle was selected to provide the −1st diffraction order and subsequent excitation of surface plasmon-polaritons at the wavelength in accordance with the equation:

$$\sin(\theta) = \pm 1 \mp m\lambda/d, \tag{1}$$

where *m* is an integer for the diffraction order, λ is the wavelength, and *d* is the period of the MPCs. Moreover, the specific θ was preferred to maximize the δ for the MPCs under study [27], while utilizing the −1st diffraction order allowed to obtain resonant features with higher efficiency compared to higher diffraction orders [28]. The experimental setup consisted of a halogen light source Mi-150 by Dolan-Jenner, two Glan–Taylor calcite prisms GT10 by Thorlabs, a system of lenses, an optomechanical chopper OCV6300F by Avesta with a modulating frequency of 344 Hz, a monochromator MS5204i by SOL Instruments, an SR830 Lock-in amplifier by Stanford Research, and a PMM02 photomultiplier tube by Thorlabs as a detector. The plane of light incidence was perpendicular to the direction of the MPCs' grooves. A focused 1 mm diameter light beam was employed during measurements to prevent the illumination of the samples' edges. The reflectivity of the samples under the influence of a magnetic field ($\Delta R = R_{+H} - R_{-H}$) was measured by modifying the setup with Helmholtz coils generating a modulation AC magnetic field (H_{AC}) applied perpendicular to the plane of light incidence. The frequency of the H_{AC} was set at 68 Hz and its strength at 250 Oe. A schematic representation of the experimental setup and the AFM image of the MPC with the 10 nm-thick $Ni_{80}Fe_{20}$ layer are shown in Fig. 1.

The δ was calculated according to the formula:

$$\delta = (\Delta R/R_0)\cdot 100\% = (\Delta U/U_0)\cdot 100\%, \quad (2)$$

where ΔU and U_0 are the detector's outputs in volts induced by the light reflected from a sample with applied saturating H_{AC} and without any applied magnetic field, respectively. The spectral dependencies of the MPCs' R_0 and δ were simulated using the Ansys Lumerical FDTD software. The simulations were carried out under the approximation of a plane wave propagating at $\theta = 68^\circ$. The dielectric permittivity tensor ε of $Ni_{80}Fe_{20}$ with off-diagonal elements ε_{xy} and ε_{yx} equal to $\pm ig$, where g is the gyration constant, was defined from the Ref. [24]. To simulate the δ spectra, MPCs' R_0 was simulated in two opposite directions of the magnetic field R_{+H} and R_{-H}, which were subsequently used to calculate δ according to the equation:

$$\delta = [2(R_{+H} - R_{-H})/(R_{+H} + R_{-H})]\cdot 100\%. \quad (3)$$

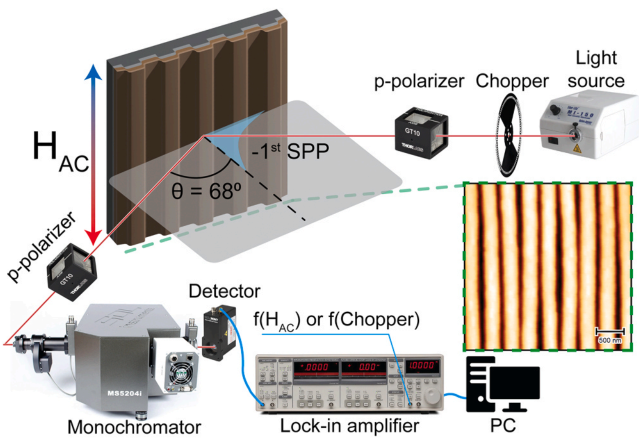

Fig. 1. The schematic representation of the setup for R_0 and δ spectroscopy. The inset shows an AFM image for the MPC with the 10 nm $Ni_{80}Fe_{20}$ layer.

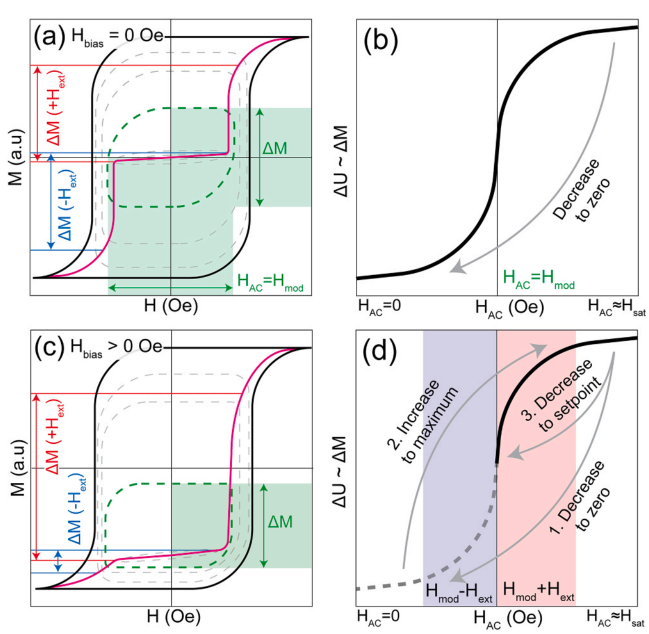

Fig. 2. Panel (a) illustrates a cyclic demagnetization of a MPC without H_{bias}. The pink line represents the normal magnetization curve. Changes in ΔM when with applied negative or positive H_{ext} are indicated with blue and red arrows. Panel (c) illustrates the demagnetization of the MPC with H_{bias}. Panel (d) demonstrates the procedure for a ΔU curve measurement and adjusting the setpoint, with red and blue areas indicating ΔU change proportional to the H_{ext}.

The optical setup for R_0 and δ measurements was also used to measure calibration ΔU curves that determine the sensitivity of the MPCs to H_{ext}. This involved the measurement of ΔU at the wavelength corresponding to the maximum δ during the cyclic demagnetization of MPCs in H_{AC}. The acquired data points were fitted with the Langevin function to determine the sensitivity as $\partial(\Delta U)/\partial(H_{AC})$. The value of H_{mod} was defined as the H_{AC} corresponding to the maximum sensitivity, whereas the maximum LoD and LoQ at H_{mod} were estimated as:

$$LoD = 3\sigma/Sensitivty, \quad (4)$$

$$LoQ = 10\sigma/Sensitivty, \quad (5)$$

where σ is a standard deviation of ΔU for 500 acquisition points. The full ΔH of MPCs was calculated by considering the H_{AC} range between $\Delta U = \Delta U(H_{AC} = H_{sat})$ - 3σ and $\Delta U = 3\sigma$. The optimal ΔH was calculated as the H_{AC} range that corresponds to 10 % of the maximum sensitivity.

The utilization of a dual-phase lock-in detection scheme implied that the measured ΔU curves were directly proportional to the susceptibility of the MPCs multiplied by the H_{AC}, or, in other words, the modulation value of MPCs' magnetization (ΔM) by H_{AC} [29,30] as shown in Fig. 2(a – b). At low frequencies, ΔU curves are consistent with the cycling demagnetization of the MPCs under a gradually decreasing DC magnetic field and fit the normal magnetization curve [23]. As depicted in Fig. 2 (a), when both DC H_{ext} and AC H_{mod} are applied to the MPC, various segments of the normal magnetization curve can be accessed, resulting in AC susceptibility variations and consequential ΔU changes. However, in this case ΔU is insensitive to the H_{ext} polarity due to the similarity of the normal magnetization curve. To reconstruct both the polarity and strength of the H_{ext}, a minor magnetization curve must be used. This allows for the adjustment of magnetization modulation and subsequent alterations in the ΔU value depending on the polarity of the applied H_{ext}, as illustrated schematically in Fig. 2(c). To access a minor magnetization curve a DC bias magnetic field (H_{bias}), significantly smaller than H_c, was simultaneously applied with H_{AC} during the ΔU curve measurement. More results regarding the demagnetization of the MPCs can be found in Refs. [19,23].

To enhance the locality and LoD of the setup, a light source was replaced with the laser module CPS635R by Thorlabs which had the operational wavelength close to the δ maximum of the optimal MPC. To ensure the time stability of the signal with a deviation of 1 – 2 % from the mean value, the setup was preliminary warmed-up for 1 hour. The collimation system was improved by using the Mitutoyo apochromatic objective MY5X-802, resulting in a reduction in the diameter of the focused light spot to 165 μm.

The following protocol outlines the steps involved in the magnetic field mapping of experimental objects. The H_{AC} was set to a saturating value of 10 Oe, followed by a gradual reduction to zero in increments of 0.01 Oe to obtain the calibration ΔU curve in the presence of a small H_{bias} of 0.1 Oe. This curve was used to determine the H_{mod}, ΔH, LoD, and LoQ after the system enhancements. Subsequently, the H_{AC} was set to the saturating value and decreased to the H_{mod} using the same increment. A schematic representation of the sequence is presented in Fig. 2(d). In the absence of H_{ext}, ΔU remains proportional to the H_{mod}. At this setpoint, any applied positive or negative DC H_{ext} up to H_{sat}, in parallel alignment with the H_{mod}, would result in an increase or decrease of the ΔU value due to the additive nature of the magnetic fields.

To obtain the magnetic field maps generated by experimental objects an automated 2-axis linear stage was employed to manipulate the positioning of objects across a square 2D plane at varying distances. This system allowed for movement within an area of up to 24×24 mm^2, with an incremental step of 0.5 mm. The precision of spatial alignment was conditioned by the linear stages' travel accuracy, which was equal to 9 μm. To accommodate the system and experimental objects positioned behind the MPC-based sensing element, instead of Helmholtz coils an arrangement of smaller electromagnets capable of generating sufficient

H_{AC} in a spacing of 4 cm was used. The outer and inner diameters of the electromagnets were 95 mm and 30 mm, respectively. The process of the magnetic field mapping was automatized within the LabView environment.

Once the setpoint was specified, an experimental object was positioned behind the MPC at various distances and moved in the 2D plane to obtain a series of 2D maps. Each map was a result of 10 separate measurements. The first experimental object was a multicore cable, characterized by a diameter of 2 mm including a 1 mm insulation layer. The direct current and voltage in the cable were 600 mA and 300 mV, respectively. The magnetic field measurements were done within a square area spanning 14.5×14.5 mm^2. The second experimental object was a planar induction coil with an outer diameter of 15 mm and 11 windings. The direct current and voltage in the coil were 55 mA and 3 V, respectively. The magnetic field measurements were done within a square area of 23×23 mm^2. The maximum magnetic field strength of both objects was analytically estimated in accordance with the Biot-Savart-Laplace law.

3. Results and discussions

One of the key parameters utilized in the assessment of the MPCs' performance as sensing elements is the full ΔH. This parameter corresponds to the range of magnetic fields that can be safely applied to the MPC without its magnetic saturation, which causes the loss of the reqired δ modulation. The straightforward way for the derivation of this parameter involves the determination of the MPCs' H_{sat} from their hysteresis loops. In accordance with our previous research, the MPCs exhibit a geometrically-driven uniaxial magnetic anisotropy, with the EMA aligned with the grooves on their surface [26]. This was also supported by the VSM hysteresis loops measured perpendicular to the samples' grooves and local in-plane hysteresis loops along the EMA in the transversely applied field, shown in Fig. S3 of the supplementary materials. A comparison between MOKE and VSM hysteresis loops' shapes, depicted in Fig. 3(a – c), showed that, contrary to the rapid magnetization of the MPCs' central parts, the magnetization process of their entire volume could be affected by the MPCs' edge defects [26]. This also was the reason of higher H_c measured with VSM method compared to the MOKE measurements except for the MPC with a 5 nm $Ni_{80}Fe_{20}$ layer. In this case, higher H_c values obtained from MOKE was attributed to the pinning of magnetic domains on the MPC's surface defects [31,32]. To account for the magnetization switching that occurs only within the central area of the MPCs' and exclude the impact of edge defects, the full ΔH was calculated using H_{sat} derived from MOKE hysteresis loops. The values of VSM and MOKE H_c as well as MOKE H_{sat}, depending on the $Ni_{80}Fe_{20}$ layer thickness, are shown in Fig. 3(d).

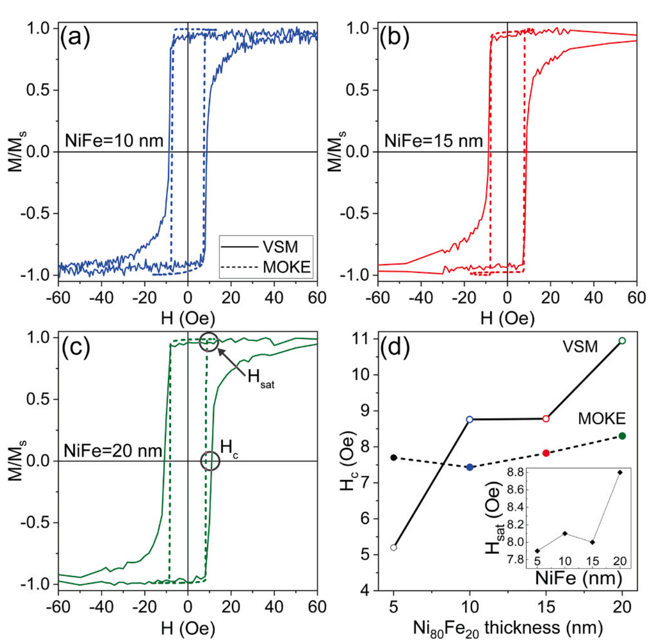

Fig. 3. (a – c) EMA VSM and MOKE hysteresis loops of the MPCs with different $Ni_{80}Fe_{20}$ layer thicknesses. (d) MPCs' H_c measured with VSM and MOKE. The inset shows H_{sat} defined from the MOKE loops. Data for the MPC based on the 5 nm $Ni_{80}Fe_{20}$ layer were taken from Ref. [24].

In comparison to the reference samples, which were flat Ag/$Ni_{80}Fe_{20}$/Si_3N_4 films with the same layers thickness, the MPCs meet the phase-matching conditions between the incident light and the propagating surface plasmon-polaritons at a resonant wavelength close to 632 nm, as reported in Refs. [27,33]. The excitation of surface plasmon-polaritons manifests itself as a local minimum in the R_0 spectra of MPCs known as the Wood anomaly, and a resonant enhancement of δ within the same wavelength range. These distinct features were observed in the R_0 and δ spectra of the MPCs shown in Fig. 4(a – c). The minimum R_0 and maximum δ, defined from experimental and simulated spectra, are shown in Fig. 4(d). The spectral position and amplitude of the R_0 minima for each MPC demonstrated a good agreement with the simulated spectra presented in Fig. S4 of the supplementary materials. The small differences in the magnitude and spectral position of δ resonant features between the experimental and simulated spectra can be attributed to minor discrepancies in the $Ni_{80}Fe_{20}$ ε_{xy} and ε_{yx} values used in simulations compared to the actual parameters of the fabricated MPCs. The MPCs' R_0 minima exhibited a non-monotonic dependence on the $Ni_{80}Fe_{20}$ layer thickness with a maximum value of 17.6 % for a thickness of 10 nm, which is 2.2 times smaller than that of the reference sample. This MPC also had the maximum δ at the wavelength of 638 nm reaching 1.24 % in comparison to the MPCs with 5, 15, and 20 nm-thick $Ni_{80}Fe_{20}$ layers providing δ of 1.07 %, 1.23 %, and 1.17 %. Compared to the reference samples, the MPCs based on 5, 10, 15, and 20 nm-thick $Ni_{80}Fe_{20}$ layers showed 3.8-, 3.5-, 3.8-, and 4.9-fold enhancement of δ at the same wavelength, respectively.

The determination of the sensitivity, H_{mod}, ΔH, LoQ, and LoD of the MPCs was accomplished through the measurement of the calibration ΔU curves in decreasing H_{AC} at a resonant wavelength of 638 nm. The calibration ΔU curves and the sensitivity are shown in Fig. 5(a). Analysis of the acquired data showed a tendency for the H_{mod} to decrease as the thickness of the $Ni_{80}Fe_{20}$ layer was reduced, mirroring a similar pattern

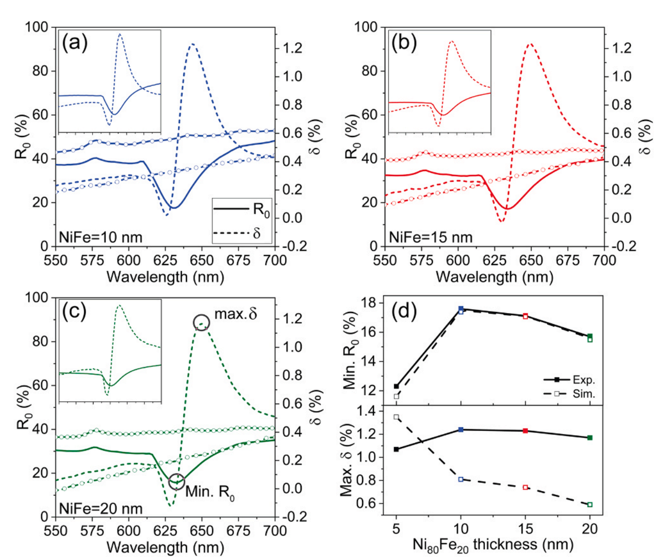

Fig. 4. (a – c) R_0 and δ spectra of reference samples (circles) and MPCs (no symbols) with different $Ni_{80}Fe_{20}$ layer thicknesses. Insets denote the simulated spectra. (d) Minimum R_0 and maximum δ obtained from experimental and simulated data. Data for the MPC based on the 5 nm $Ni_{80}Fe_{20}$ layer were taken from Ref. [24].

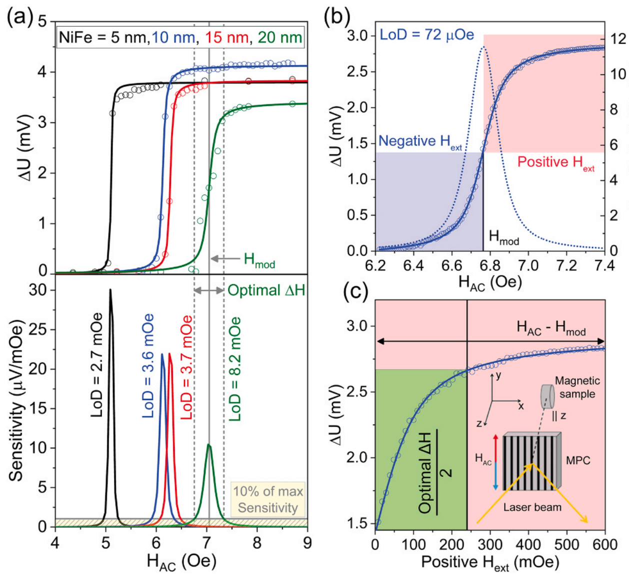

Fig. 5. (a) The calibration ΔU curves and sensitivity of the MPCs with different $Ni_{80}Fe_{20}$ layer thickness. Circles and solid lines denote experimental data points and Langevin fit curves. (b) The calibration ΔU curve (solid line) and sensitivity (dotted line) of the MPC with a 10 nm $Ni_{80}Fe_{20}$ layer. Marked areas correspond to the ΔU signal proportional to the H_{ext}. (c) Dependence of the ΔU on the H_{ext} for the MPC with a 10 nm $Ni_{80}Fe_{20}$ layer. The green area depicts the optimal ΔH for positive H_{ext}. The inset shows a schematic image of the magnetic field mapping experiment.

observed for the H_c, measured with the VSM. This correlation was also in agreement with the demagnetization dynamics of the studied type of MPCs [23]. Owing to the nonlinearity of the calibration ΔU curves, in addition to the full ΔH, an optimal ΔH was identified within which each MPC could measure magnetic field with a sufficient sensitivity. It is also important to note, that the parameters of the MPCs can vary significantly when measured at the edges rather than in central regions. This variability is due to the impact of edge defects on the magnetization process, as illustrated by VSM hysteresis loops. Additionally, changing the angle of light incidence or utilizing higher diffraction orders can result in the δ reduction leading to a subsequent decrease in *LoD* and sensitivity, while preserving the ΔH, which is determined solely by the MPCs' magnetic properties.The calculated H_{mod}, maximum sensitivity, full and optimal ΔH, *LoD*, and *LoQ* for the fabricated MPCs are shown in Table 1.

At first appraisal, the MPC based on a 5 nm-thick $Ni_{80}Fe_{20}$ layer was the most suitable for the evaluation of DC H_{ext} due to the best H_{mod} of 5.1 Oe, a maximum sensitivity of 30.1 μV/mOe, and a *LoD* of 2.7 mOe. However, this MPC had the smallest optimal ΔH of 208.1 mOe. To meet the criteria of optimality, a MPC should exhibit all parameters at sufficient levels without compromising any of them. Notably, the MPC with a 10 nm $Ni_{80}Fe_{20}$ layer achieved a higher ΔH of 325.8 mOe while maintaining other parameters at average levels among the studied MPCs. One way to further increase the ΔH for MPCs with the same composition involves increasing their period, although this may result in reduced sensitivity [25]. Thus, due to the highest δ value, optimal sensitivity and ΔH, the MPC with a 10 nm $Ni_{80}Fe_{20}$ layer was suitable for magnetic field measurements.

Table 1
H_{mod}, maximum sensitivity, ΔH, *LoD*, and *LoQ* values for the MPCs with different $Ni_{80}Fe_{20}$ layer thickness.

$Ni_{80}Fe_{20}$ thickness (nm)	5	10	15	20
H_{mod} (Oe)	5.1	6.1	6.3	7.0
Max. sensitivity (μV/mOe)	30.1	21.9	22.0	10.5
Full ΔH (Oe)	1.018	1.134	0.841	1.655
Optimal ΔH (mOe)	208.1	325.8	298.2	585.8
LoD (mOe)	2.7	3.6	3.7	8.2
LoQ (mOe)	9.0	12.5	12.6	27.4

Conventional magneto-optical magnetic field sensors based on flat thin magnetic films typically provide a *LoD* of 1 – 10 Oe [34], with some examples achieving values as high as 100 mOe [35,36], which remains two orders of magnitude lower than the results obtained for the studied MPCs. Recent advancements in magneto-optical sensing were done utilizing the longitudinal magnetophotonic intensity effect to detect magnetic fields with *LoD* of 24 μOe at a full ΔH of approximately 750 mOe [17]. While the MPCs in the current study offer a smaller *LoD* and comparable ΔH values, the utilization of a reflectance geometry compared to the transmission geometry in Ref. [17] may be advantageous in applications requiring proximity between the sensing element and the object of interest. Future enhancements in this technology might focus on detecting a three-dimensional trajectory of an MPC magnetization, potentially enabling sensitivities on the order of 10 fOe [10,11].

After modification of the measuring system with a laser module as a light source and an apochromatic objective as a collimation system, the calibration ΔU curve and sensitivity of the MPC based on a 10 nm $Ni_{80}Fe_{20}$ layer were remeasured. The obtained dependencies are shown in Fig. 5(b). The assembled setup allowed measurements with the locality of 259 μm^2, *LoD* of 72 μOe, and *LoQ* of 240 μOe, while increasing the H_{mod} to 6.8 Oe and optimal ΔH to 479.4 mOe. However, the maximum sensitivity of the system reached a lower value of 11.6 μV/mOe due to the reduced light flux reflected from the MPC. The correlation between H_{ext} and ΔU was determined by analyzing the dependence of the ΔU on the H_{AC} - H_{mod}, that is illustratively shown in Fig. 5 (c). The assembled setup was then used to obtain magnetic field maps on a 2D plane for a multicore cable and a planar induction coil, as shown in Fig. 6. Magnetic field maps at different distances can be found in Fig. S5 and Fig. S6 of the supplementary materials.

As expected, both the multicore cable and planar induction coil exhibited distinct magnetic field patterns. The magnetic field of the multicore cable has a circular trajectory around the axis of the wire,

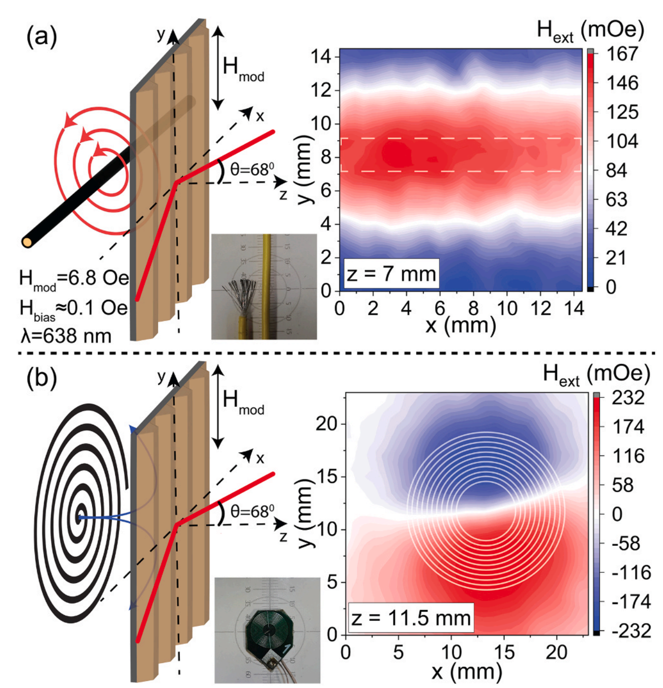

Fig. 6. Experimental objects, measurement geometries, and magnetic field maps for the (a) multicore cable and the (b) planar induction coil. Measurements were carried out using the MPC with the 10 nm thick $Ni_{80}Fe_{20}$ layer. H_{mod} is the modulation magnetic field, H_{bias} is a bias DC magnetic field, and H_{ext} is an external DC magnetic field, generated by objects at the distance z. The position of the objects relative to the spatial coordinates is outlined in the maps.

attaining its maximum intensity at the surface and decreasing inversely proportional to the distance. Similarly, the planar induction coil can be represented as a system of wires curved in circular loops, each carrying the same current. The resulting magnetic field pattern was formed by the sum of individual windings' fields and was symmetrical around the coil's axis. The maximum measured H_{ext} of the multicore cable at the distance of 7 mm was 166.5 mOe, which was close to the analytical estimation of 150 mOe. Likewise, the magnetic field map of the planar induction coil was in good agreement with analytical estimations, showing a maximum H_{ext} of 222 mOe at the distance of 11.5 mm comparable to the analytically calculated value of 214 mOe. A comparison between the maximum H_{ext} values at varying distances obtained using the experimental set-up and calculations is provided in Table S1 and Table S2 of the supplementary materials. The resemblance observed between experimental and analytical evaluations validates the reliability of the measuring technique and its applicability in exploring magnetic configurations of electromagnetic and micromagnetic systems.

4. Conclusion

The contactless magnetooptical magnetic field sensing elements based on 5 – 20 nm $Ni_{80}Fe_{20}$ films have been presented in this work, and their potential for the DC magnetic field visualization has been analyzed. The thickening of the $Ni_{80}Fe_{20}$ layer led to an increase in coercive and saturation fields, responsible for the higher modulation field and measuring field range of studied magnetoplasmonic crystals. The dependence of both the reflectivity and transverse Kerr effect at the resonant wavelength on the thickness of the $Ni_{80}Fe_{20}$ layer was observed to exhibit a non-monotonic trend, with extremums appearing at a thickness of 10 nm. The magnetoplasmonic crystal based on the 10 nm-thick $Ni_{80}Fe_{20}$ layer yielded the maximum transverse Kerr effect value, reaching 1.24 %, and a reflectivity of 17.6 %. This magnetoplasmonic crystal allowed to achieve a sensitivity of 21.9 μV/mOe, a limit-of-detection of 3.6 mOe, and the optimal measuring field range of 325.8 mOe expanding to 1.134 Oe at the cost of a sensitivity drop below 10 % of the maximum value. Further incorporation of the magnetoplasmonic crystal with 10 nm-thick $Ni_{80}Fe_{20}$ layer a sensing element of a magnetic field mapping setup allowed to achieve increased spatial locality of 259 μm^2 and sensitivity of 11.6 μV/mOe. The acquisition of 2D magnetic field maps from a multicore cable and a planar induction coil illustrated a good alignment with estimated values, proving the utility of proposed elements for magnetic field visualization. This study establishes an approach for the development of cost-effective and compact magnetic field sensing elements based on $Ni_{80}Fe_{20}$ magnetoplasmonic crystals, tailored to specific sensitivity and measuring field range requirements. Such sensing elements may find applications for facilitating remote and non-destructive characterization of electromagnetic or micromagnetic structures.

Funding

This work was financially supported by the Ministry of Science and Higher Education of the Russian Federation (075–02–2024–1430)

Declaration of Competing Interest

The authors declare that they have no known competing financial interests or personal relationships that could have appeared to influence the work reported in this paper.

Data availability

Data will be made available on request.

Acknowledgements

The authors acknowledge the "Center for development of gifted children" (Kaliningrad) for the provision of the SEM/EDX equipment.

Appendix A. Supporting information

Supplementary data associated with this article can be found in the online version at doi:10.1016/j.sna.2024.115552.

References

[1] A. Grosz, M.J. Haji-Sheikh, S.C. Mukhopadhyay, High Sensitivity Magnetometers (eds.), Springer International Publishing, Cham, 2017, https://doi.org/10.1007/978-3-319-34070-8.

[2] M.A. Khan, J. Sun, B. Li, A. Przybysz, J. Kosel, Magnetic sensors-A review and recent technologies, Eng. Res. Express 3 (2021) 022005, https://doi.org/10.1088/2631-8695/ac0838.

[3] B. Brajon, E. Gasparin, G. Close, A Benchmark of Integrated Magnetometers and Magnetic Gradiometers, IEEE Access 11 (2023) 115635–115643, https://doi.org/10.1109/ACCESS.2023.3325035.

[4] N. Aslam, H. Zhou, E.K. Urbach, M.J. Turner, R.L. Walsworth, M.D. Lukin, H. Park, Quantum sensors for biomedical applications, Nat. Rev. Phys. 5 (2023) 157–169, https://doi.org/10.1038/s42254-023-00558-3.

[5] A. Fabricant, I. Novikova, G. Bison, How to build a magnetometer with thermal atomic vapor: a tutorial, N. J. Phys. 25 (2023) 025001, https://doi.org/10.1088/1367-2630/acb840.

[6] A. Kimel, A. Zvezdin, S. Sharma, S. Shallcross, N. De Sousa, A. García-Martín, G. Salvan, J. Hamrle, O. Stejskal, J. McCord, S. Tacchi, G. Carlotti, P. Gambardella, G. Salis, M. Münzenberg, M. Schultze, V. Temnov, I.V. Bychkov, L.N. Kotov, N. Maccaferri, D. Ignatyeva, V. Belotelov, C. Donnelly, A.H. Rodriguez, I. Matsuda, T. Ruchon, M. Fanciulli, M. Sacchi, C.R. Du, H. Wang, N.P. Armitage, M. Schubert, V. Darakchieva, B. Liu, Z. Huang, B. Ding, A. Berger, P. Vavassori, The 2022 magneto-optics roadmap, J. Phys. D: Appl. Phys. 55 (2022) 463003, https://doi.org/10.1088/1361-6463/ac8da0.

[7] A. Zvezdin, Modern magnetooptics and magnetooptical materials, n.d.

[8] J. Qin, S. Xia, W. Yang, H. Wang, W. Yan, Y. Yang, Z. Wei, W. Liu, Y. Luo, L. Deng, L. Bi, Nanophotonic devices based on magneto-optical materials: recent developments and applications, Nanophotonics 11 (2022) 2639–2659, https://doi.org/10.1515/nanoph-2021-0719.

[9] C. Rizal, M.G. Manera, D.O. Ignatyeva, J.R. Mejía-Salazar, R. Rella, V.I. Belotelov, F. Pineider, N. Maccaferri, Magnetophotonics for sensing and magnetometry toward industrial applications, J. Appl. Phys. 130 (2021) 230901, https://doi.org/10.1063/5.0072884.

[10] A.E. Rogachev, P.M. Vetoshko, N.A. Gusev, M.A. Kozhaev, A.R. Prokopov, V. V. Popov, D.V. Dodonov, A.G. Shumilov, A.N. Shaposhnikov, V.N. Berzhansky, A. K. Zvezdin, V.I. Belotelov, Vector magneto-optical sensor based on transparent magnetic films with cubic crystallographic symmetry, Appl. Phys. Lett. 109 (2016) 162403, https://doi.org/10.1063/1.4964887.

[11] D.O. Ignatyeva, G.A. Knyazev, A.N. Kalish, A.I. Chernov, V.I. Belotelov, Vector magneto-optical magnetometer based on resonant all-dielectric gratings with highly anisotropic iron garnet films, J. Phys. D: Appl. Phys. 54 (2021) 295001, https://doi.org/10.1088/1361-6463/abfb1c.

[12] S. Arakelyan, O. Galstyan, H. Lee, A. Babajanyan, J.-H. Lee, B. Friedman, K. Lee, Direct current imaging using a magneto-optical sensor, Sens. Actuators A: Phys. 238 (2016) 397–401, https://doi.org/10.1016/j.sna.2016.01.002.

[13] L. Dorosinskiy, S. Sievers, Magneto-Optical Indicator Films: Fabrication, Principles of Operation, Calibration, and Applications, Sensors 23 (2023) 4048, https://doi.org/10.3390/s23084048.

[14] V.I. Belotelov, I.A. Akimov, M. Pohl, V.A. Kotov, S. Kasture, A.S. Vengurlekar, A. V. Gopal, D.R. Yakovlev, A.K. Zvezdin, M. Bayer, Enhanced magneto-optical effects in magnetoplasmonic crystals, Nat. Nanotech 6 (2011) 370–376, https://doi.org/10.1038/nnano.2011.54.

[15] J.Y. Chin, T. Steinle, T. Wehlus, D. Dregely, T. Weiss, V.I. Belotelov, B. Stritzker, H. Giessen, Nonreciprocal plasmonics enables giant enhancement of thin-film Faraday rotation, Nat. Commun. 4 (2013) 1599, https://doi.org/10.1038/ncomms2609.

[16] N. Maccaferri, A. Gabbani, F. Pineider, T. Kaihara, T. Tapani, P. Vavassori, Magnetoplasmonics in confined geometries: Current challenges and future opportunities, Appl. Phys. Lett. 122 (2023) 120502, https://doi.org/10.1063/5.0136941.

[17] G.A. Knyazev, P.O. Kapralov, N.A. Gusev, A.N. Kalish, P.M. Vetoshko, S. A. Dagesyan, A.N. Shaposhnikov, A.R. Prokopov, V.N. Berzhansky, A.K. Zvezdin, V. I. Belotelov, Magnetoplasmonic crystals for highly sensitive magnetometry, ACS Photonics 5 (2018) 4951–4959, https://doi.org/10.1021/acsphotonics.8b01135.

[18] R. Cichelero, M.A. Oskuei, M. Kataja, S.M. Hamidi, G. Herranz, Unexpected large transverse magneto-optic Kerr effect at quasi-normal incidence in magnetoplasmonic crystals, J. Magn. Magn. Mater. 476 (2019) 54–58, https://doi.org/10.1016/j.jmmm.2018.12.036.

[19] V.K. Belyaev, D.V. Murzin, A.G. Kozlov, A.A. Grunin, A.S. Samardak, A.V. Ognev, A.A. Fedyanin, M. Inoue, V.V. Rodionova, Engineering of optical, magneto-optical and magnetic properties of nickel-based one-dimensional magnetoplasmonic

crystals, Jpn. J. Appl. Phys. 59 (2020) SEEA08, https://doi.org/10.35848/1347-4065/ab71df.
[20] V.K. Belyaev, D.V. Murzin, N.N. Perova, A.A. Grunin, A.A. Fedyanin, V. V. Rodionova, Permalloy-based magnetoplasmonic crystals for sensor applications, J. Magn. Magn. Mater. 482 (2019) 292–295, https://doi.org/10.1016/j.jmmm.2019.03.052.
[21] M.A. Kiryanov, A.Yu Frolov, I.A. Novikov, P.A. Kipp, P.K. Nurgalieva, V.V. Popov, A.A. Ezhov, T.V. Dolgova, A.A. Fedyanin, Surface profile-tailored magneto-optics in magnetoplasmonic crystals, APL Photonics 7 (2022) 026104, https://doi.org/10.1063/5.0072698.
[22] R.S. Singh, P.K. Sarswat, From fundamentals to applications: The development of magnetoplasmonics for next-generation technologies, Mater. Today Electron. 4 (2023) 100033, https://doi.org/10.1016/j.mtelec.2023.100033.
[23] V.K. Belyaev, V.V. Rodionova, A.A. Grunin, M. Inoue, A.A. Fedyanin, Magnetic field sensor based on magnetoplasmonic crystal, Sci. Rep. 10 (2020) 7133, https://doi.org/10.1038/s41598-020-63535-1.
[24] D.V. Murzin, A.Yu Frolov, K.A. Mamian, V.K. Belyaev, A.A. Fedyanin, V. V. Rodionova, Low coercivity magnetoplasmonic crystal based on a thin permalloy film for magnetic field sensing applications, Opt. Mater. Express 13 (2023) 171, https://doi.org/10.1364/OME.478112.
[25] D. Murzin, V.K. Belyaev, F. Groß, J. Gräfe, N. Perov, V. Komanicky, V. Rodionova, Magnetic field sensing elements made of quasi-trapezoidal magnetoplasmonic crystals based on thin permalloy films, J. Magn. Magn. Mater. 588 (2023) 171398, https://doi.org/10.1016/j.jmmm.2023.171398.
[26] V.K. Belyaev, A.G. Kozlov, A.V. Ognev, A.S. Samardak, V.V. Rodionova, Magnetic properties and geometry-driven magnetic anisotropy of magnetoplasmonic crystals, J. Magn. Magn. Mater. 480 (2019) 150–153, https://doi.org/10.1016/j.jmmm.2019.02.032.
[27] A.A. Grunin, A.G. Zhdanov, A.A. Ezhov, E.A. Ganshina, A.A. Fedyanin, Surface-plasmon-induced enhancement of magneto-optical Kerr effect in all-nickel subwavelength nanogratings, Appl. Phys. Lett. 97 (2010) 261908, https://doi.org/10.1063/1.3533260.
[28] A.V. Kats, M.L. Nesterov, A.Yu Nikitin, Excitation of surface plasmon-polaritons in metal films with double periodic modulation: anomalous optical effects, Phys. Rev. B 76 (2007) 045413, https://doi.org/10.1103/PhysRevB.76.045413.
[29] D. Drobac, Z. Marohnic, I. Zivkovic, M. Prester, The role of lock-in phase setting in ac susceptibility measurement, Rev. Sci. Instrum. 84 (2013) 054708, https://doi.org/10.1063/1.4807752.
[30] I.N. Bhatti, A.K. Pramanik, Laboratory-constructed instrumentation for the characterization of first and higher-order harmonics of dynamic susceptibility: a low cost AC susceptometer, Instrum. Exp. Tech. 66 (2023) 103–110, https://doi.org/10.1134/S0020441223010050.
[31] M. Veis, L. Beran, M. Zahradnik, R. Antos, L. Straka, J. Kopecek, L. Fekete, O. Heczko, Magneto-optical spectroscopy of ferromagnetic shape-memory Ni-Mn-Ga alloy, J. Appl. Phys. 115 (2014) 17A936, https://doi.org/10.1063/1.4867754.
[32] J. Gräfe, G. Schütz, E.J. Goering, Coercivity scaling in antidot lattices in Fe, Ni, and NiFe thin films, J. Magn. Magn. Mater. 419 (2016) 517–520, https://doi.org/10.1016/j.jmmm.2016.06.052.
[33] A.A. Grunin, A.V. Chetvertukhin, T.V. Dolgova, A.A. Ezhov, A.A. Fedyanin, Magnetoplasmonic crystals based on commercial digital discs, J. Appl. Phys. 113 (2013) 17A946, https://doi.org/10.1063/1.4801525.
[34] L. Knauss, S. Woods, A. Orozco, Current imaging using magnetic field sensors, Microelectron. Fail. Anal. Desk-.-. Ref. 5 (2004) 303–311.
[35] EURAMET EMPIR Programme Project 15SIB06 "Nano-Scale Traceable Magnetic Field Measurements" Final Publishable Report, (2019). ⟨www.euramet.org⟩ (accessed April 18, 2024).
[36] Matesy MO systems: Magneto-optical visualization technology and systems, (n.d.). ⟨https://matesy.de/en/⟩ (accessed April 18, 2024).

Murzin D.V. received his MSc degree with honours in physics from Immanuel Kant Baltic Federal University, Russian Federation, in 2021. Currently, he is a PhD student at the research and education center "Smart Materials and Biomedical Applications" at Immanuel Kant Baltic Federal University. His research area focuses on optical and magneto-optical effects in nanostructured ferromagnetic materials.

Dr. Belyaev V.K. graduated from Immanuel Kant Baltic Federal University in 2012 and successfully his PhD thesis on physics of magnetism in Lomonosov Moscow State University in 2022. At the moment BVK is a head of laboratory of magneto-optical studies in Research and Education Center "Smart materials and Biomedical Applications" and his main research interests focuses on magnetization dynamics and enhancement of magneto-optical effects studies.

Mamian K.A received his BSc degree with honours in physics from Lomonosov Moscow State University, Russia in 2023. Currently, he is a MSc student at the Nanophotonics Department at Lomonosov Moscow State University, Russia. His research focuses on the optical and magneto-optical properties of hybrid metal-dielectric and metallic nanostructures.

Dr. Groß F. received his M. Sc. degree in physics from the University of Stuttgart, Germany in 2017. Afterwards, he did his Ph. D. in physics at the Max Planck Institute for Intelligent Systems in Stuttgart and graduated from the University of Stuttgart in 2022, followed by an additional year of postdoc.

Dr. Gräfe J earned his PhD from University of Stuttgart, Germany, in 2016. His research area focuses on magnetization dynamics and magnonics on the nano scale.

Dr. Frolov A.Y. received his diploma in physics with honors from Lomonosov Moscow State University in 2013, and received his PhD in laser physics from the same university in 2023. Currently, he works as a researcher at the Nanophotonics Department of Lomonosov Moscow State University. His research focuses on static and ultrafast magneto-optical effects in nanophotonic structures and scanning near-field optical microscopy.

Prof. Andrey Fedyanin received his diploma in physics with honours from Lomonosov Moscow State University, and received his PhD in laser physics (1997) and Doctor of science degree (Habilitation) (2009) from the same university. He is currently the head of the Nanophotonics Department at Lomonosov Moscow State University, where his research focuses on nonlinear, magneto-optical, and ultrafast properties of nanophotonic devices.

Dr. Rodionova V.V. earned her PhD from Lomonosov Moscow State University, Russian Federation, in 2010. She now serves as the director of the research and education center "Smart Materials and Biomedical Applications" at Immanuel Kant Baltic Federal University. Her research focuses on magnetic films and nanostructures, amorphous and soft magnetic materials, biphase magnetic microwires, as well as domain wall dynamics and high-frequency behavior properties of amorphous materials.